Supplemental information for "The MJO on the equatorial beta-plane: an eastward propagating Rossby wave induced by meridional moisture advection"

N.B. the figures in this supplementary material are prefixed with the letter S. Referents without a prefix denote figures and tables in the main text.

1 Parameter sensitivity of the ERW horizontal structure

1.1 Precipitation-moisture phase relationship

The ERW horizontal structure displayed in Fig. 4 is also sensitive to parameteric choices, in addition to zonal wavenumber. This is demonstrated using Fig. S1, which shows changes to the zonal wavenumber 2 ERW horizontal structure in response to perturbations in m_{eff} and ϵ_q. The primary focus here is the slight quadrature component in the ERW moisture-precipitation phase relationship. This is seen in Fig. S1a for the reference solution. As discussed in Section 4b, this relationship is different for observed MJO composites, which instead show a stronger moisture-precipitation in-phase relationship. In Figs. S1c and d, m_{eff} is halved (=0.05) from its reference value, while the other parameter values are retained from Table 1. Comparing Figs. S1a–b to Figs. S1c–d shows that the ERW precipitation and column moisture perturbations are more in-phase when m_{eff} is smaller. The reference value for the moisture sensitivity of convection (ϵ_q) was informed by the empirical analysis in Ahmed et al. (2020), but is still subject to uncertainties due to a single vertical profile assumed for moisture variations. The consequences of this uncertainty for ERW moisture-precipitation phase relationships are made clear in Figs. S1e–h. In these figures, m_{eff} is fixed at 0.05 while ϵ_q is perturbed. As ϵ_q^{-1} increases above its reference value of 6 h, the precipitation gets more in-phase with column-integrated moisture (Figs. S1e and g), and more in line with observed MJO composites. Parameteric choices could therefore explain some of the differences between the observed MJO and the $n = 1$ ERW moisture-precipitation phase relationships. The ratio between peak moisture and temperature perturbations for the structures in Figs. S1d and f are 4.0 and 6.3 respectively, which bracket the corresponding estimate for the observed MJO (~ 5). The moisture-temperature ratio for the structure in Fig. S1h is 8.9. These solutions are all QE modes (with moisture-temperature ratios $\leq 1.5\epsilon_t/\epsilon_q$). However, these modes are also situated farther away from pure QE and slightly closer to the moisture mode regime when compared to the structure with the same zonal wavenumber in Fig. S1b.
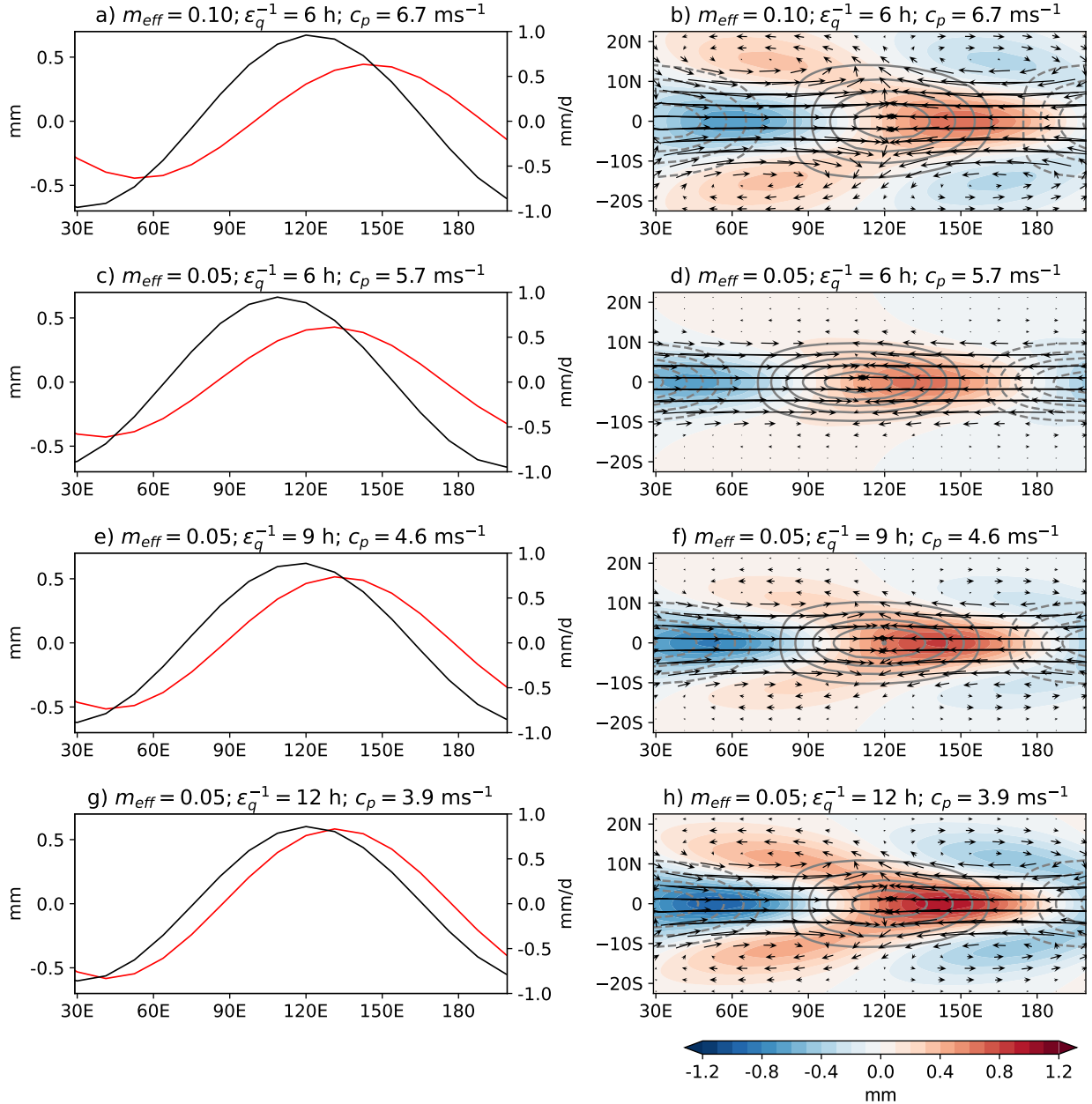
Figure S1: Left column: column-integrated moisture (red curve; units of mm) and precipitation (black curve; units of mm/d) perturbations averaged between 10 N-S for the zonal wavenumber 2 ERW in different parameter regimes. Right column: the corresponding horizontal structures of the column-integrated moisture (colors), precipitation (grey line contours) and horizontal wind (black vectors). Each row depicts a solution in a different parameter regime, whose m_{eff} and ϵ_q values along with the mode phase speed (c_p) are shown in the panel title. The top row (panels a and b) depicts the reference solution. Note that the y-axis range (~ 20 N-S) for panels in the right column is different from Fig. 4 (~ 30 N-S).

Another interesting feature in Fig. S1 is the narrowed meridional extent of the eigenfunctions in

Figs. S1d, f and h when compared to Fig. S1b. When m_{eff} is fixed at 0.05, and the moisture sensitivity of convection is increased—moving from the fourth to the second row of Fig. S1— the eigenfunctions are increasingly confined to the near-equatorial region of 10 N–S. The off-equatorial gyres progressively diminish in magnitude such that the horizontal velocities have but a weak meridional component in Fig. S1d. This behavior is suggestive of a transition from the $n = 1$ ERW to the $v = 0$ Kelvin wave, which was also hypothesized from the dispersion relationships in Figs. 11c and d.

1.2 Equatorial versus off-equatorial temperature anomalies

Fig. S2 shows the ERW horizontal structures for two parameter regimes. These differ from the reference regime in the value of ϵ_q (Figs. S2a and b), and that of m_{eff} (Figs. S2c and d). The focus here is the strength of the off-equatorial temperature perturbation. In both these regimes, the strength of the off-equatorial temperature perturbations are stronger than the equatorial peak. This is in contrast to Fig. 4 and more in line with observed MJO composites (e.g., Hendon and Liebmann 1994). Both these parameter tweaks (weaker moisture sensitivity of convection and a larger m_{eff} value) decrease the precipitation strength per unit moisture perturbation. A slightly weaker precipitation response therefore weakens the near-equatorial temperature perturbation (which primarily arises to maintain the zonal wavenumber 2 ERW near a state of QE). This figure serves to further highlight that parameteric choices could explain some of the discrepancies between the ERW horizontal structure and observed MJO composites.
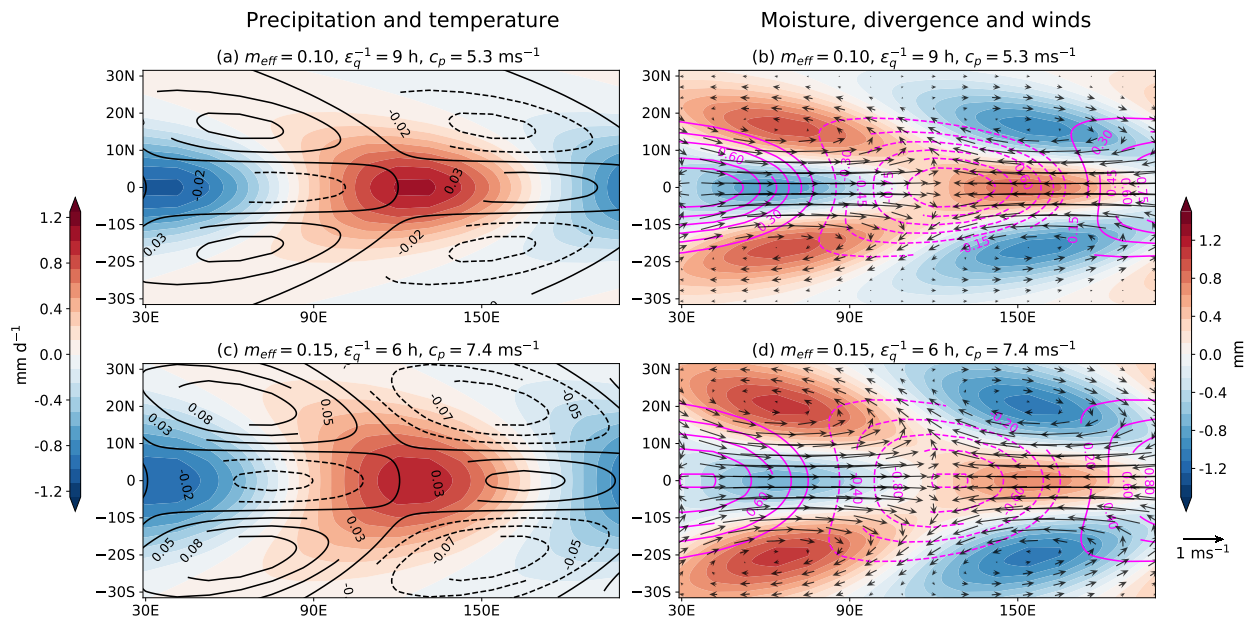

Figure S2: As in Fig. 4 but for two different parameter combinations. In panels a and b, the moisture sensitivity timescale (=9 h) is longer than in the reference regime. In panels c and d, the m_{eff} value (=0.15) is larger than in the reference regime.

2 Full near-equatorial growth budget

The near-equatorial growth budget in Fig. 7 presents the combined effects of both the cloud-radiative effects $\langle Q_r \rangle$ and the vertical MSE advection $\omega_1 m M_s$. The individual impacts of these two terms is shown in Fig. S3. The cloud-radiative feedback term is the largest positive contributors to ERW MSE growth, while vertical advection is the largest sink of ERW MSE. As the zonal wavenumber increases, the impact of both these terms on the MSE budget also increases. This is because the vertical velocity is more in-phase with the MSE perturbations for large zonal wavenumbers (as discussed in Section 5c). Since the radiative heating is also mostly in-phase with ω_1, the positive impacts of $\langle Q_r \rangle$ also increase with zonal wavenumber. In fact, the combined effects of $\omega_1 m M_s$ and $\langle Q_r \rangle$ can be written more compactly by first considering the WTG estimate of convective heating from (17):

$$\omega_1 M_s \approx -\langle Q_c \rangle (1 + r), \tag{S1}$$

where $\langle Q_c \rangle$ is the convective heating written in un-parameterized form. Since $\langle Q_r \rangle = r \langle Q_c \rangle$—from (12)—we can write:

$$\omega_1 m M_s + \langle Q_r \rangle \approx -\langle Q_c \rangle \left[m(1 + r) - r \right] = -\langle Q_c \rangle m_{eff}, \tag{S2}$$

where the definition of m_{eff} from (21) has been used. Fig. S4 compares the effects of $\omega_1 m M_s + \langle Q_r \rangle$ and its estimate from (S2). Clearly, the estimate from (S2) is a good approximation for $\omega_1 m M_s + \langle Q_r \rangle$. This implies that $\omega_1 m M_s$ and $\langle Q_r \rangle$ evolve in a near constant fraction of $\frac{-r}{m(1+r)}$ for the ERW.
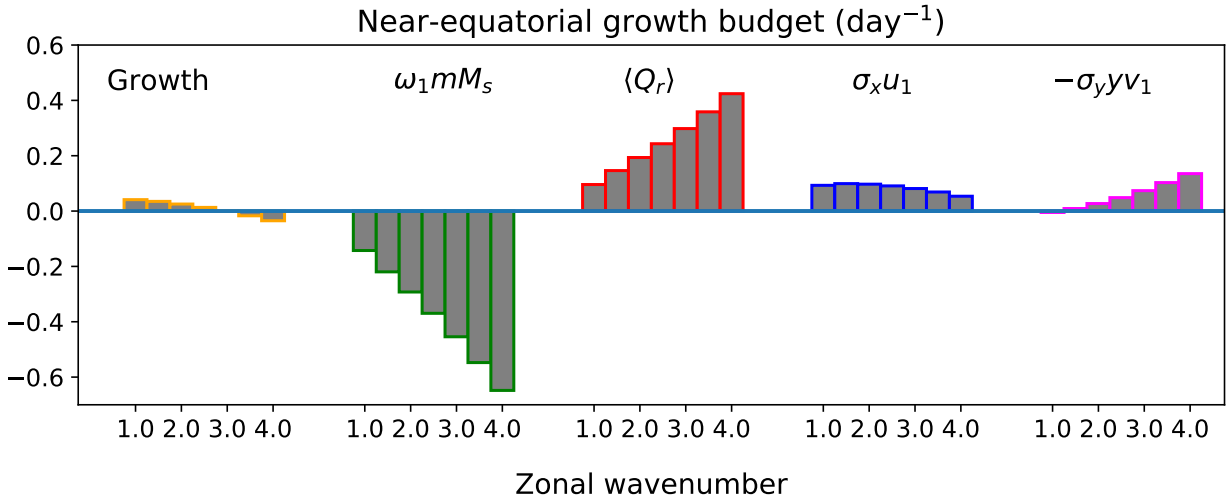

Figure S3: As in Fig. 7 but with the impacts of $\langle Q_r \rangle$ and $\omega_1 m M_s$ shown separately.

Interestingly, the estimate in (S2) also implies that the WTG balance holds in the temperature equation, (17). However, the temperature tendency term cannot be neglected, because i) the wind field perturbations are coupled to temperature perturbations in the momentum equations (14) and (15), and ii) convection is highly sensitive to temperature perturbations—from (11)—so even small temperature perturbations can influence the ERW precipitation field.
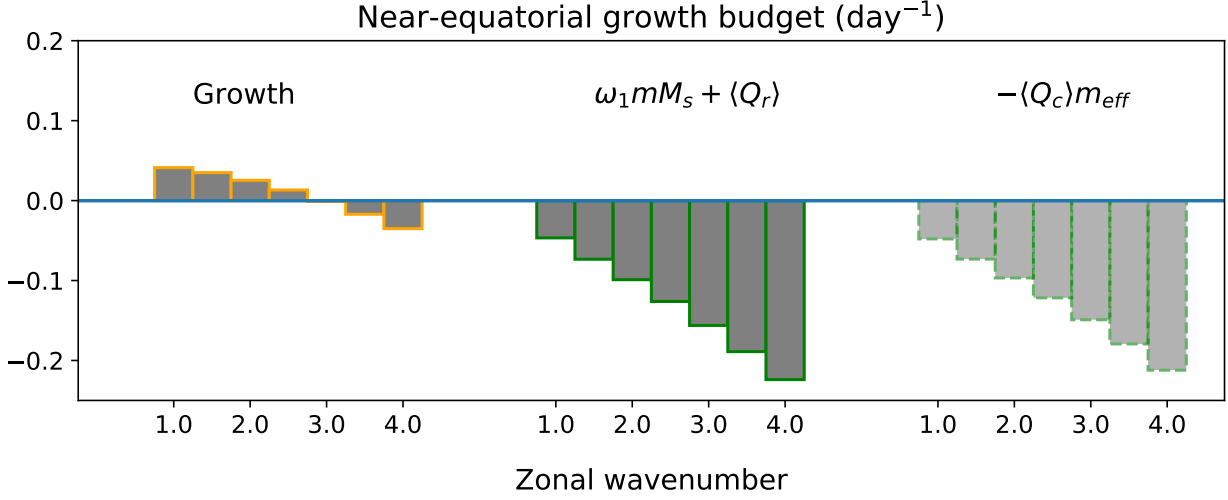
4

Figure S4: As in Fig. S3 but comparing $\omega_1 mMs + \langle Q_r \rangle$ to its estimate from (S2).
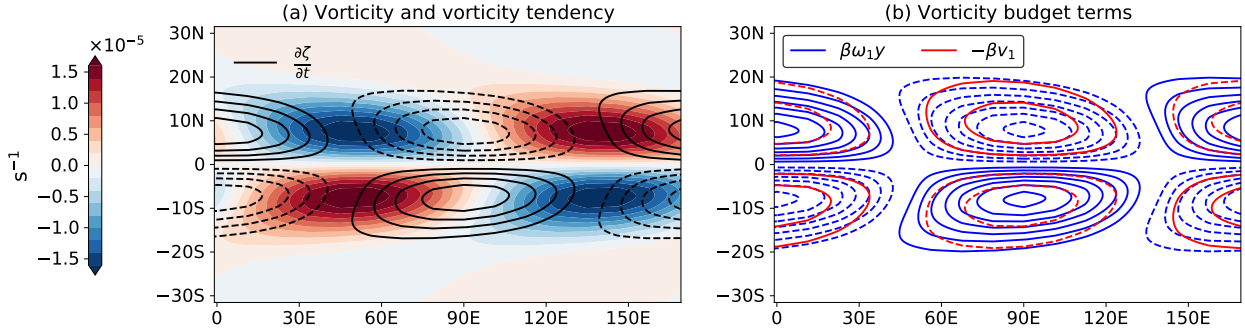
3 The ERW vorticity budget

Figure S5: a) The ERW vorticity (colors) and vorticity tendency (line contours); negative vorticity contours are dashed. b) The terms of the ERW vorticity budget: vortex stretching ($\beta\omega_1 y$) and planetary vorticity advection ($-\beta v_1$).

The ERW is analyzed using the MSE budget in Section 5c. However, a complementary perspective of the ERW dynamics is available from the vorticity budget. The vertical vorticity tendency equation for the linearized model can be constructed using (14), (15) and (16):

$$\partial_t \zeta_1 = \beta\omega_1 y - \beta v_1, \tag{S3}$$

where the vertical component of the vorticity is:

$$\zeta_1 = \partial_x v_1 - \partial_y u_1.$$

The first term on the right hand side of (S3) ($\beta\omega_1 y$) is the vortex stretching term and the second term ($-\beta v_1$) is the planetary vorticity advection term. Fig. S5a shows the ERW vorticity

and vorticity tendency terms. The vorticity tendency is clearly phased to induce eastward propagation of the vorticity anomalies. Decomposing the vorticity tendency term into its components (Fig. S5b) shows that the vortex stretching term induces eastward propagation of the vorticity anomalies, while the planetary vorticity advection induces westward propagation. From a vorticity perspective, the ERW therefore propagates eastward because the vortex stretching overcomes the beta-effect. This interpretation is consistent with the mechanism posited in Hayashi and Itoh (2017).

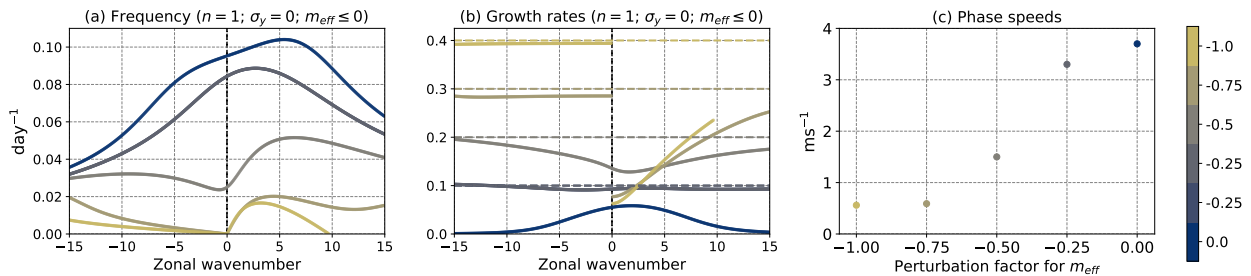# 4   The negative gross moist stability regime

Figure S6: a) Frequencies and b) growth rates obtained from the $m_{eff} \leq 0$ perturbation experiment with $\sigma_y = 0$. c) Phase speeds for the zonal wavenumber 2 eastward propagating $n = 1$ mode as a function of the m_{eff} perturbation factor. The colors denote the different perturbation factors whose values are indicated in the colorbar. The dashed horizontal lines in b) are the asymptotic moisture mode growth rates.

A pertinent parameter regime for moist tropical disturbances is one with negative m_{eff} (Raymond and Fuchs 2009; Sobel and Maloney 2013; Adames and Kim 2016). As stated in Section 6a, when $m_{eff} < 0$ and $\sigma_y > 0$, there are no valid ERW solutions. However, low-frequency eastward and westward propagating $n = 1$ modes do emerge when the meridional moisture gradient is absent ($\sigma_y = 0$) and when $m_{eff} < 0$, as shown in Figs. S6. These modes are unstable (Figs. S6b) largely because convection amplifies MSE anomalies when $m_{eff} < 0$; although positive growth rates are still seen at planetary scales when $m_{eff} = 0$. Since convection neither amplifies nor damps the MSE anomalies when $m_{eff} = 0$, the positive growth rates in this case arise from the effects of σ_x and σ_y.

As m_{eff} values become more negative, the largest growth rates for the eastward propagating mode preferentially occur at the smallest scales. For $m_{eff} \leq -0.75$ times the reference value, a discontinuity between growth rates for the eastward and westward propagating modes emerges at wavenumber zero (Figs. S6b). For these m_{eff} values, the westward propagating modes also display scale-independent growth for all wavenumbers, suggesting a moisture mode regime at all scales. This conclusion is supported by the fact that the moisture mode growth rate ($-m_{eff}\epsilon_q$) is a reasonable estimator of these wavenumber-independent growth rates. When $m_{eff} = -0.75$ times the reference value, the growth rate for the eastward propagating $n = 1$ mode also asymptotes to

the moisture mode growth rate at large zonal wavenumbers (not shown). The zonal wavenumber 2 phase speeds for the eastward propagating mode (Figs. S6c) diminish with increasingly negative m_{eff}, and are nearly stationary (< 1 ms^{-1}) when $m_{eff} \leq -0.75$.

Overall, this experiment shows that slow eastward propagating $n = 1$ modes can exist when $m_{eff} < 0$. However, these modes do not show planetary scale-selection in the absence of other scale-selectors such as diffusion. The MJO-like mode reported in Emanuel (2020) is destabilized by cloud-radiative feedbacks, which is suggestive of a negative m_{eff} regime. The vortex-stretching mechanism of Hayashi and Itoh (2017) is also possibly relevant in explaining how the $n = 1$ mode propagates eastward in the negative m_{eff} regime without a meridional moisture gradient.

References

Adames, Á. F., and D. Kim, 2016: The MJO as a dispersive, convectively coupled moisture wave: Theory and observations. *Journal of the Atmospheric Sciences*, **73 (3)**, 913–941, doi:10. 1175/JAS-D-15-0170.1.

Ahmed, F., Á. F. Adames, and J. D. Neelin, 2020: Deep convective adjustment of temperature and moisture. *Journal of the Atmospheric Sciences*, **77 (6)**, 2163–2186.

Emanuel, K., 2020: Slow modes of the equatorial waveguide. *Journal of the Atmospheric Sciences*, **77 (5)**, 1575–1582, doi:10.1175/JAS-D-19-0281.1.

Hayashi, M., and H. Itoh, 2017: A new mechanism of the slow eastward propagation of unstable disturbances with convection in the tropics: Implications for the MJO. *Journal of the Atmospheric Sciences*, **74 (11)**, 3749–3769.

Hendon, H. H., and B. Liebmann, 1994: Organization of convection within the madden-julian oscillation. *Journal of Geophysical Research: Atmospheres*, **99 (D4)**, 8073–8083.

Raymond, D. J., and Ž. Fuchs, 2009: Moisture modes and the madden–julian oscillation. *Journal of Climate*, **22 (11)**, 3031–3046.

Sobel, A., and E. Maloney, 2013: Moisture modes and the eastward propagation of the MJO. *Journal of the Atmospheric Sciences*, **70 (1)**, 187–192, doi:10.1175/JAS-D-12-0189.1.